NASA
Technical
Memorandum

NASA TM-100358

OBLIQUE HYPERVELOCITY IMPACT RESPONSE OF DUAL-SHEET STRUCTURES

By William P. Schonberg and Roy A. Taylor

Materials and Processes Laboratory
Science and Engineering Directorate

January 1989

(NASA-TM-100358) OBLIQUE HYPERVELOCITY IMPACT RESPONSE OF DUAL-SHEET STRUCTURES (NASA) 44 p CSCI 20K

N89-21246

Unclas
G3/37 0200731

National Aeronautics and
Space Administration

George C. Marshall Space Flight Center

MSFC - Form 3190 (Rev. May 1983)

TECHNICAL REPORT STANDARD TITLE PAGE

1. REPORT NO.	2. GOVERNMENT ACCESSION NO.	3. RECIPIENT'S CATALOG NO.
NASA TM- 100358		

4. TITLE AND SUBTITLE	5. REPORT DATE
Oblique Hypervelocity Impact Response of Dual-Sheet Structures	January 1989
	6. PERFORMING ORGANIZATION CODE
7. AUTHOR(S)	8. PERFORMING ORGANIZATION REPORT #
William P. Schonberg* and Roy A. Taylor	
9. PERFORMING ORGANIZATION NAME AND ADDRESS	10. WORK UNIT NO.
George C. Marshall Space Flight Center Marshall Space Flight Center, Alabama 35812	11. CONTRACT OR GRANT NO.
	13. TYPE OF REPORT & PERIOD COVERED
12. SPONSORING AGENCY NAME AND ADDRESS	Technical Memorandum
National Aeronautics and Space Administration Washington, D.C. 20546	14. SPONSORING AGENCY CODE Code S

15. SUPPLEMENTARY NOTES

Prepared by Materials and Processes Laboratory, Science and Engineering Directorate.

16. ABSTRACT

This report describes the results of a continuing investigation of the phenomena associated with the oblique hypervelocity impact of spherical projectiles onto multi-sheet aluminum structures. A series of equations that quantitatively describes these phenomena is obtained through a regression of experimental data. These equations characterize observed ricochet and penetration damage phenomena in a multi-sheet structure as functions of geometric parameters of the structure and the diameter, obliquity, and velocity of the impacting projectile. Crater damage observed on the ricochet witness plates is used to determine the sizes and speeds of the ricochet debris particles that caused the damage. It is observed that the diameter of the most damaging ricochet debris particle can be as large as 40 percent of the original particle diameter and can travel at speeds between 24 percent and 36 percent of the original projectile impact velocity. The equations necessary for the design of shielding panels that will protect external systems from such ricochet debris damage are also developed. The dimensions of these shielding panels are shown to be strongly dependent on their inclination and on their circumferential distribution around the spacecraft. It is concluded that obliquity effects of high-speed impacts must be considered in the design of any structure exposed to the meteoroid and space debris environment.

*Professor of Mechanical Engineering, Mechanical Engineering Department, University of Alabama in Huntsville.

17. KEY WORDS	18. DISTRIBUTION STATEMENT
Oblique Hypervelocity Impact Response Ricochet Phenomena	Unclassified – Unlimited

19. SECURITY CLASSIF. (of this report)	20. SECURITY CLASSIF. (of this page)	21. NO. OF PAGES	22. PRICE
Unclassified	Unclassified	43	NTIS

For sale by National Technical Information Service, Springfield, Virginia 22151

ACKNOWLEDGMENTS

The authors wish to acknowledge the support of the NASA/ASEE Summer Faculty Fellowship Program along with Michael Freeman, the University of Alabama Director, and Ernestine Cothran, the MSFC Program Co-Director. The authors wish to express their appreciation to Raymond Gause, Chief of the Engineering Physics Division, for his suggestions in the development of the ricochet debris containment shield system, and to Hubert Smith of the Laboratory Support Branch for conducting the impact testing which made this report possible. The authors' gratitude is also extended to Jane Schonberg for her assistance in the preparation of this report.

TABLE OF CONTENTS

	Page
INTRODUCTION	1
RESULTS SUMMARY FROM PREVIOUS INVESTIGATION	2
EXPERIMENTAL PROCEDURE AND RESULTS	3
BUMPER PLATE HOLE ANALYSIS	9
PENETRATION DEBRIS CENTER-OF-MASS TRAJECTORY ANALYSIS	11
PENETRATION DEBRIS CLOUD CONE ANGLES	12
RICOCHET ANGLE ANALYSIS	14
RICOCHET PARTICLE SIZE AND VELOCITY ANALYSIS	15
DESIGN OF EXTERNAL DEBRIS CONTAINMENT SHIELDS	19
Development of Shield Concept	19
Design Equations	21
Design Procedure	27
Examples	28
CONCLUSIONS AND RECOMMENDATIONS	28
REFERENCES	30
APPENDIX	33
Penetration Depth Equations	33
Crater Diameter Equations	34
Notation	35
Material Properties	35

LIST OF ILLUSTRATIONS

Figure	Title	Page
1.	Test configuration and parameter definitions	3
2.	Oblique hypervelocity impact: Pre-event stage	4
3.	Oblique hypervelocity impact: Formation of richocet debris cloud	5
4.	Oblique hypervelocity impact: Formation of penetration debris cloud	5
5.	Oblique hypervelocity impact: Spread of ricochet and penetration debris clouds	6
6.	Bumper plate hole dimensions: Test data compared with regression equation predictions	10
7.	Penetration fragments trajectories: Test data compared with regression equation predictions	13
8.	Ricochet fragments trajectories: Test data compared with regression equation predictions	14
9.	Space station module orientation	19
10.	Space station module cross-section with containment shield parameters	20
11.	Meteoroid/space debris trajectories	21
12.	Containment shield geometry for design condition No. 1	22
13.	Containment shield geometry for design condition No. 2	25

LIST OF TABLES

Table	Title	Page
1.	Impact Test Database: Penetration and Ricochet Angles	7
2.	Impact Test Database: Bumper Plate Hole Dimensions	8
3.	Regression Analysis of Bumper Hole Dimension Data, Error Summary	10
4.	Angle Data Regression Analysis, Error Summary	12
5.	Measured Penetration Depths and Crater Diameters	17
6.	Calculated Particle Diameters and Velocities	17
7.	Average Ricochet Particle Diameters and Velocities as a Function of Original Projectile Obliquity and Diameter	18
8.	Prediction Errors Using Calculated Particle Diameters and Velocities	18
9.	Panel Length and Thickness as a Function of Panel Inclination and Shield Element Separation	28

TECHNICAL MEMORANDUM

OBLIQUE HYPERVELOCITY IMPACT RESPONSE OF DUAL-SHEET STRUCTURES

INTRODUCTION

All spacecraft with a mission duration of more than a few days are susceptible to impacts by meteoroid and pieces of space debris. Such impacts are expected to occur at extremely high speeds and are expected to strike the spacecraft structure at oblique angles. High-speed oblique impacts are known to produce penetration and ricochet debris and can therefore damage internal as well as external flight-critical systems of the spacecraft. Either type of damage can in turn lead to catastrophic failure of the spacecraft and loss of life. Uncontained ricochet debris also increases the contamination of the orbital environment and can pose a threat to future missions into that environment. The design of a spacecraft for a long-duration mission must take into account the possibility of such impacts and their effects on the integrity of the entire structure. Protective systems for habitable portions and for external structural subsystems must be included in its design.

Protection against penetration for crew compartments and modules has traditionally consisted of a bumper plate that is placed at a small distance away from the main wall of the compartment or module. This concept was first proposed by Whipple [1] and has been studied extensively in the last few years as a means of reducing the penetration threat of hypervelocity impacts [2-15]. In the design process, bumper and wall plate thicknesses are iterated against weight and protection considerations to arrive at a final configuration.

In a recent investigation of hypervelocity impact [16], it was demonstrated that oblique high-speed impacts generate a tremendous volume of ricochet debris, especially for impact trajectories above 45 deg. In fact, for trajectory obliquities beyond 60 deg, the amount of penetration damage in a multi-sheet test specimen was observed to be minimal when compared to the damage sustained by the ricochet witness plate in the specimen. Unfortunately, previous investigations of oblique impact discuss only penetration phenomena and make little or no mention of damage induced by ricochet debris [2,9,15,17,18]. It has become clear that the damage potential of ricochet debris is very great, and that the creation of such debris is a dangerous phenomenon that deserves further attention.

The objectives of the research program performed under this fellowship were as follows: (1) to continue and extend the work begun in the first investigation by expanding the application of the equations previously developed; (2) to develop new equations for phenomena not discussed previously; (3) to analyze the formation and damage potential of ricochet debris and to develop a means of containing its spread. The results of this research program are presented in this report.

In the first section, the results of the previous investigation are reviewed. Suggestions for future research efforts made at its conclusion are also reviewed in light of the objectives of the present research program. In the next section, a review of the experimental procedure used in the oblique hypervelocity impact testing of multi-sheet specimens is presented. A complete set of impact test results is

presented and reviewed. In the following sections, new equations governing the response of multi-sheet structures to oblique hypervelocity impact are presented. The damage potential of ricochet debris particles is analyzed by determining the sizes and speeds of typical ricochet debris particles. Equations and methodology for the design of shielding panels to protect external structural system elements are also developed. Several examples of panel design are presented. Finally, conclusions are made based on the data analysis of the preceding sections. Recommendations for future experimental and analytical investigations of hypervelocity impact are also presented.

RESULTS SUMMARY FROM PREVIOUS INVESTIGATION

Several important conclusions and recommendations were made at the completion of this authors' first investigation of oblique hypervelocity impact phenomena [16]. These are reviewed below.

First, there exists a critical angle of obliquity. Projectiles with angles of obliquity less than this critical angle produce significant damage to the interior pressure wall and little damage to a ricochet witness plate. Projectiles with trajectory obliquities greater than the critical angle produce minimal damage to the pressure wall plate, but generate ricochet debris that causes major damage to a ricochet witness plate. This critical angle is estimated to have a value between 60 and 65 deg. The existence of such an angle can have serious consequences on the design and placement of external subsystems such as instrumentation units on spacecraft that are developed for long-duration missions in the meteoroid and space debris environment.

Second, 99 percent of the ricochet debris particles generated traveled along trajectories never more than 30 deg away from the bumper plate, regardless of the original angle of impact. The most serious ricochet damage was found to occur within an angle of 15 deg with respect to the plane of the bumper plate, also regardless of impact angle. For original trajectory obliquities greater than 60 deg, thin ricochet witness plates were completely perforated at the bumper plate/ricochet witness plate interface. In general, ricochet damage was found to increase with increases in original trajectory obliquity, original impact velocity, and the size of the original incident projectile.

Third, future experimental testing of oblique impact should be conducted with ricochet witness plates sufficiently thick so that little or no spalling or perforation occurs. With this stipulation, all the crater damage produced by ricochet particles can be used with thick plate equations to perform a detailed study of the damage potential of ricochet debris particles.

Fourth, future experimental investigations should also be conducted with larger diameter projectiles and specimen plates made from different thicknesses and materials. In this manner, the testing will better simulate the orbital space debris environment and the effect of bumper thickness on penetration and ricochet damage can be analyzed. Use of a wide variety of diameters and thicknesses will also serve to expand the applicability of current empirical expressions.

Fifth, more impact testing is needed at higher angles of obliquity to complement the large number of tests that have been performed at smaller angles (i.e., less than 45 deg). In light of the existence of a critical obliquity angle near 60 deg, these tests are essential to be able to fully understand the oblique impact process.

The test program developed for the current investigation focused on the recommendations made in the last three paragraphs. Tests were performed using larger projectiles, thicker ricochet witness plates, and various bumper plate thicknesses. The majority of the tests were performed at high angles of obliquity, although data from several previous normal impact tests were also included in some aspects of the analyses. The effect of the new data on existing equations will be addressed in subsequent sections.

EXPERIMENTAL PROCEDURE AND RESULTS

The oblique hypervelocity impact testing of multi-sheet specimens was done at the Space Debris Simulation Facility of the Materials and Processes Laboratory at the Marshall Space Flight Center. The facility consists of a light gas gun with a 12.7-mm (0.5-in.) launch tube capable of launching 2.5 to 12.7 mm (0.1 to 0.5 in.) projectiles of mass 4 to 300 mg (0.009 to 0.661 lbs) at velocities of 2 to 8 km/sec (6,500 to 26,246 ft/sec). Projectile velocity measurements were accomplished via pulsed X-ray, laser diode detectors, and a hall photographic station. This facility is fully described in Reference 19. A drawing of the multi-sheet specimen set-up is shown in Figure 1.

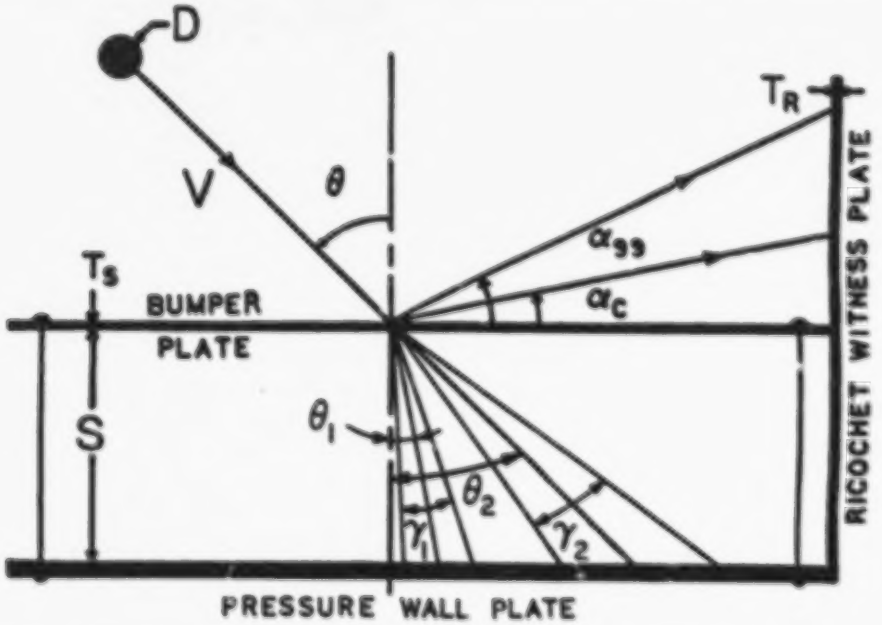

Figure 1. Test configuration and parameter definitions.

In each test, a spherical projectile of diameter D and velocity V impacted a bumper plate of thickness t_s at an angle of obliquity θ. The projectile was shattered upon impact and created an elliptical hole in the bumper plate. Some secondary projectile and bumper plate fragments were sprayed upon the pressure wall plate a distance S away while some fragments ricocheted and struck the ricochet witness plate (thickness t_r).

The angles θ_1, θ_2, γ_1, and γ_2 are "perforation angles." The angles θ_1 and θ_2 denote the trajectories of the centers of mass of bumper and "in-line" penetration fragments, respectively; the angles γ_1 and γ_2 represent the spread of these fragments. The angles α_c and α_{99} are "ricochet angles" and denote the trajectory of the center of mass of the ricochet fragments and the angle below which lie 99 percent of the ricochet fragments, respectively.

The formation and growth of penetration and ricochet debris clouds are clearly visible in Figures 2 through 5. These figures show the various stages of the oblique impact process beginning with a pre-event photograph (Fig. 2). In Figure 3, a ricochet debris cloud consisting of projectile and plate fragments is the first to form. The penetration debris cloud is subsequently produced by further plate fragmentation. Its motion is initially directed along the outward normal of the reverse side of the plate (Fig. 4). The impact event progresses and the remainder of the projectile fragments exit the rear of the plate. The penetration debris cloud then acquires an additional component of motion parallel to the rear surface of the plate. The net result is that the penetration debris cloud begins to move in a direction similar to that of the original projectile (Fig. 5). All photographs courtesy of Johnson Space Center (JSC).

The configurations of the test specimens and the conditions of impact were chosen to simulate the conditions of space debris impact as closely as possible and still remain within the realm of experimental feasibility. Kessler [20] states that the average mass density for pieces of orbital space debris less than 10 mm (0.3937 in.) in diameter is approximately 2.8 gm/cm^3, which is approximately the same as the density of aluminum. Thus, the projectiles used were solid 1100 aluminum spheres with diameters ranging from 4.75 to 9.2 mm (0.187 to 0.375 in.).

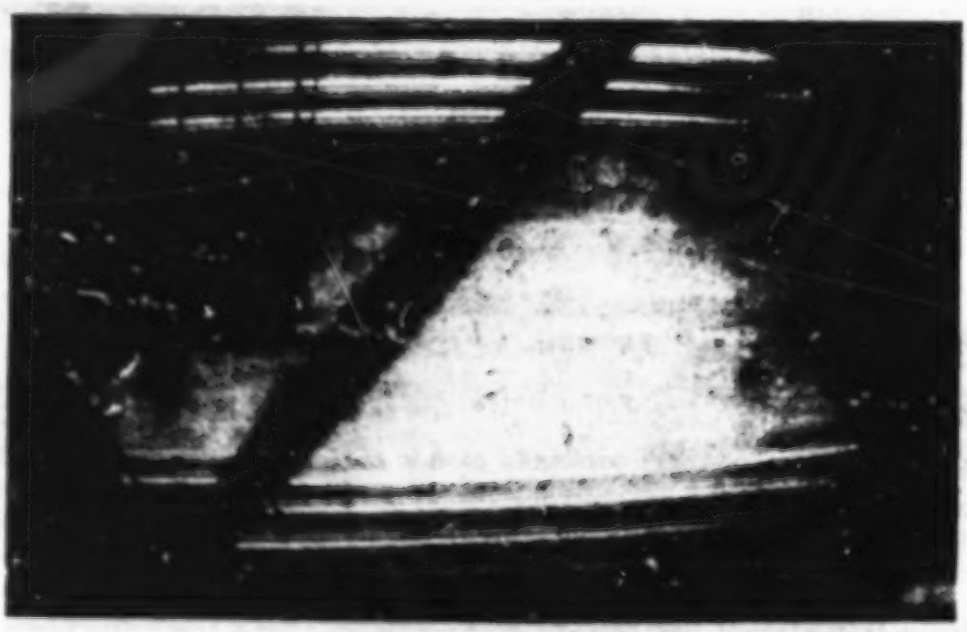

Figure 2. Oblique hypervelocity impact: Pre-event stage.

ORIGINAL PAGE IS
OF POOR QUALITY

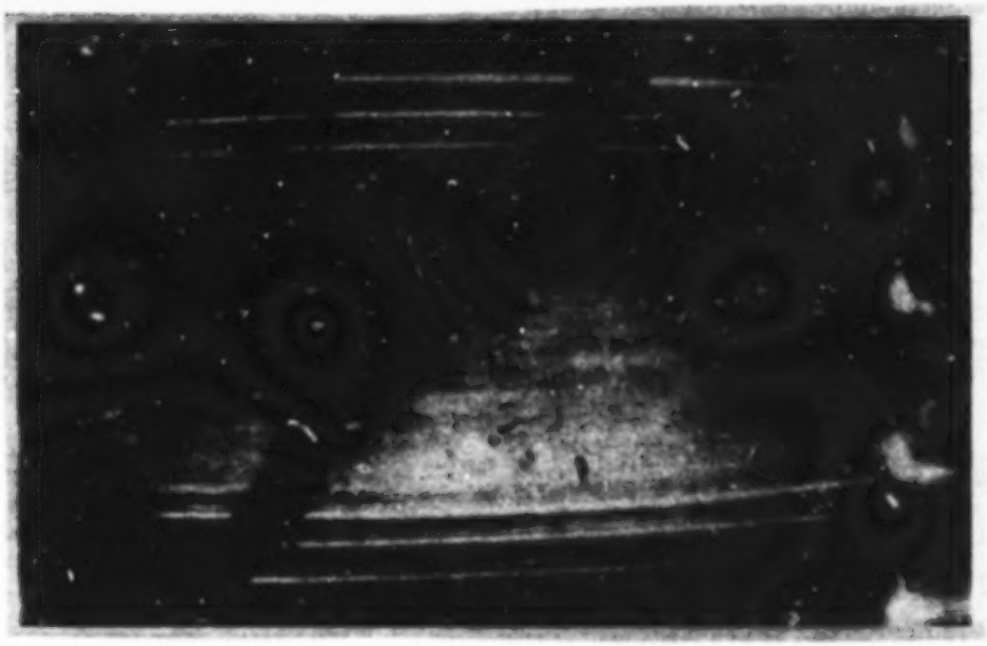

Figure 3. Oblique hypervelocity impact: Formation of ricochet debris cloud.

ORIGINAL PAGE IS
OF POOR QUALITY

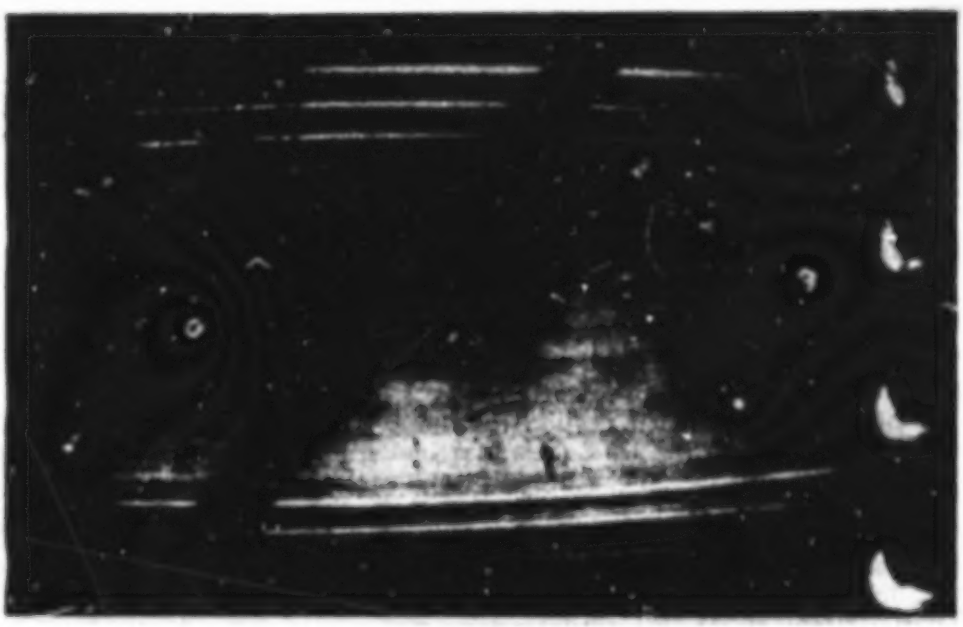

Figure 4. Oblique hypervelocity impact: Formation of penetration debris cloud.

Figure 5. Oblique hypervelocity impact: Spread of ricochet and penetration debris clouds.

The bumper, pressure wall, and ricochet witness plates were made of 6061-T6, 2219-T87, and 2219-T87 aluminum, respectively. The thicknesses of the bumper plates were varied from 0.8128 to 0.032 mm (0.032 to 0.080 in.); those of the ricochet witness plates were varied from 2.54 to 25.4 mm (0.1 to 1.0 in.). Pressure wall plate thickness was held constant at 3.175 mm (0.125 in.). The bumper and pressure wall plates were separated by a constant distance of 101.6 mm (4.0 in.). The obliquity of the impact was varied from 30 to 75 deg, while the impact velocities ranged from 5.0 to 8.0 km/sec (16,400 to 26,246 ft/sec). Data from several normal impacts were also used in the analysis of bumper plate holes.

A total of 30 oblique tests and 10 normal tests were used to study penetration and ricochet phenomena. The full database derived from these tests is presented in Tables 1 and 2. In Table 1, the angles θ_1 and θ_2 were obtained by estimating the locations of the centers of mass of the bumper plate framents and "in-line" projectile fragments on the pressure wall plate. The cone angles γ_1 and γ_2 were obtained by measuring the width of the damage cluster in the direction of the line of flight and by determining its location with respect to the edge of the pressure wall plate ahead of the cluster. The angle α_c was obtained by determining the vertical location of the center of mass of the ricochet debris based on the vertical distribution of the holes, craters, etc., formed by the debris. The angle α_{99} was determined based on the height below which lay 99 percent of the holes, craters, etc., formed by the ricochet debris. In Table 2, the minimum and maximum dimensions of the bumper plate hole in an oblique impact (D_{min} and D_{max}) as well as the hole diameters for normal impacts (D) were measured directly from the bumper plates.

ORIGINAL PAGE IS
OF POOR QUALITY

TABLE 1. IMPACT TEST DATABASE: PENETRATION AND RICOCHET ANGLES

Test No.	V (km/sec)	d (mm)	θ (deg)	θ_1 (deg)	θ_2 (deg)	γ_1 (deg)	γ_2 (deg)	α_c (deg)	$\alpha_{2/3}$ (deg)
EH1A	7.07	7.95	30	****	24.8	****	56.3	****	****
EH1B	6.96	7.95	45	10.9	38.1	42.3	30.7	15.5	29.2
EH1C	7.14	7.95	60	9.6	50.0	46.6	16.9	11.2	27.6
EH1D	7.18	7.95	75	4.7	26.9	57.1	****	7.9	27.1
EHAP	6.82	7.95	75	5.0	22.0	55.7	****	9.3	28.7
EHAA	6.93	7.95	75	4.7	22.2	47.8	****	9.5	30.1
EHAB	6.91	7.95	75	5.0	19.9	55.9	****	7.3	24.7
EHBP	7.22	6.35	75	4.3	21.8	48.7	****	6.6	26.0
EHCP	7.58	4.75	75	4.7	20.9	38.6	****	8.2	25.6
106I	6.84	8.89	60	11.3	47.1	43.4	26.5	****	****
106A	6.66	9.53	60	9.2	48.4	47.4	16.9	****	****
135C	6.76	6.35	30	****	24.0	****	53.0	****	****
135D	6.93	6.35	30	****	27.0	****	53.3	****	****
136A	6.25	6.35	55	10.7	43.5	43.9	20.9	8.7	23.3
136B	7.30	6.35	55	10.1	41.8	41.7	23.5	11.9	28.3
136C	6.67	6.35	55	11.0	38.2	44.5	24.3	12.9	28.4
150A	7.08	6.35	45	10.0	39.0	39.6	28.4	11.0	24.0
157A	7.40	4.75	60	9.3	36.0	42.4	21.2	8.0	22.0
162A	6.49	4.75	30	****	21.0	****	64.8	****	****
162B	5.03	4.75	30	****	27.0	****	52.7	****	****
208F	6.24	4.75	45	8.0	31.0	29.4	31.0	8.0	21.0
208E	6.48	6.35	65	9.0	47.0	43.5	11.7	8.0	20.0
209D	7.40	6.35	65	****	****	****	****	11.0	27.0
230C	5.16	6.35	45	10.0	34.0	34.3	23.7	11.0	26.0
230D	5.59	6.35	45	10.0	37.0	34.8	24.8	10.0	25.0
230E	6.62	6.35	45	10.0	32.0	33.0	28.3	12.0	25.0
231C	6.59	7.95	65	8.7	55.7	47.1	10.2	8.4	20.4
231D	7.26	7.95	65	10.2	49.7	48.5	20.1	9.7	23.0
EHRP1	6.87	7.95	60	10.6	46.5	52.9	22.6	10.6	23.6
EHRP2	6.80	7.95	65	11.0	64.4	49.3	9.4	8.7	19.1

ORIGINAL PAGE IS
OF POOR QUALITY

TABLE 2. IMPACT TEST DATABASE: BUMPER PLATE HOLE DIMENSIONS

Test No.	V (km/sec)	d (mm)	θ (deg)	D_{min} (mm)	D_{max} (mm)	Eccentricity	D (mm)
EH1A	7.07	7.95	30	16.0	17.0	1.06	****
EH1B	6.96	7.95	45	16.5	20.0	1.22	****
EH1C	7.14	7.95	60	16.5	24.9	1.51	****
EH1D	18	7.95	75	14.5	36.1	2.49	****
EHAP	6.82	7.95	[illegible]	13.0	33.0	2.53	****
EHAA	6.93	7.95	75	13.2	33.5	2.54	****
EHAB	6.91	7.95	[illegible]	13.2	33.5	2.54	****
EHBP	7.22	6.35	75	10.9	23.1	2.09	****
EHCP	7.58	4.75	[illegible]	10.0	18.0	1.82	****
006A	6.95	6.35	0	****	****	1.00	15.0
013B	6.15	[illegible]	0	****	****	1.00	14.0
033	7.21	6.35	0	****	****	[illegible]	13.2
033C	5.53	6.35	0	****	****	1.00	11.2
035C	5.72	8.89	0	****	****	1.00	16.0
102	7.20	7.62	0	****	****	1.00	18.0
1061	6.84	8.89	60	18.8	29.0	1.54	****
106A	6.66	9.53	60	19.8	[illegible]	1.64	****
107B	6.82	[illegible]	0	****	****	[illegible]	18.5
135C	6.76	6.35	30	[illegible]	14.2	1.08	****
135D	6.93	6.35	30	[illegible]	14.2	1.08	****
136A	6.25	6.35	55	14.0	18.3	1.31	****
136B	7.30	6.35	55	14.0	20.1	1.44	****
136C	6.67	6.35	55	13.5	17.0	1.26	****
150A	7.08	6.35	45	14.2	18.0	1.26	****
157A	7.40	4.75	60	13.7	17.3	1.26	****
162A	6.49	4.75	30	11.9	14.0	1.18	****
162B	5.03	4.75	30	9.9	11.7	1.17	****
206F	6.24	4.75	45	11.7	13.5	1.16	****
208E	6.48	6.35	65	13.0	21.0	1.61	****
209D	7.40	6.35	65	14.5	19.6	1.36	****
213B	5.90	7.95	0	****	****	1.00	16.5
228B	6.75	7.95	0	****	****	1.00	12.7
228D	6.65	6.35	0	****	****	[illegible]	11.2
230C	5.16	6.35	45	12.4	16.0	1.28	****
230D	5.59	6.35	45	13.5	16.3	1.22	****
230E	6.62	6.35	45	14.2	17.5	1.25	****
231C	6.59	7.95	65	16.5	31.0	1.87	****
231D	7.26	7.95	65	16.5	25.9	1.57	****
EHRP1	6.87	7.95	60	16.5	29.0	1.74	****
EHRP2	6.80	7.95	65	16.0	33.0	2.19	****

ORIGINAL PAGE IS
OF POOR QUALITY

A detailed qualitative description of the various processes involved in an oblique high-speed impact, including photographs of the various damage mechanisms, may be found in References 15, 16, 21, and 22. Visual inspection of the new impact test specimens revealed a variety of phenomena that were basically consistent with these previous observations.

BUMPER PLATE HOLE ANALYSIS

Elastodynamic theory predicts that as a hypervelocity projectile strikes a plate, the projectile and the portion of the plate surrounding the impact site will break up into many fragments [23]. A portion of the fragments will ricochet while the remainder will travel along the general direction of the original projectile toward the pressure wall plate. In order to estimate the damage potential of the ricochet and penetration frements, it is necessary to know the total volume of debris generated by the impact. A good estimate of the bumper plate fragment volume can be obtained by multiplying the area of the hole formed during the impact by the thickness of the bumper plate. Inspection of the test specimens revealed the bumper plate hole to be elliptical with the elongation in the direction of the original projectile trajectory. The bumper plate hole area can be, therefore, approximated as the product of the maximum hole dimension and the minimum hole dimension.

Although the smaller hole dimension was previously observed to be independent of obliquity, inspection of the bumper holes in the new test specimens revealed an increasing dependence on obliquity, especially in the high obliquity specimens. Furthermore, the original equations for the maximum dimension of the bumper plate hole did not correlate well with experimental data for very large angles of obliquity. The objectives of the analyses in this task were to (1) modify the existing equation for D_{min} by including a dependence on trajectory obliquity, and (2) improve the accuracy of the current equation for D_{max}, especially in the high obliquity regime. In addition, it was also decided to extend the applicability of both equations to include normal, as well as oblique, high-speed impacts.

The new equations were obtained through a standard multiple linear regression of the hole dimension data with the following results:

$$D_{min}/d = 2.825(V/C)^{1.043} \cos^{0.283}\theta(t_s/d)^{0.782} + 1.91 \quad (1)$$

$$D_{max}/d = 1.250(V/C)^{0.851} e^{1.064\theta}(t_s/d)^{0.672} + 1.40 \quad (2)$$

where C is the speed of sound in the bumper plate material and θ is in radians. The averages and standard deviations of the prediction errors of the regression model are presented in Table 3 (columns 1 and 2, respectively). A measure of the accuracy of the regression equations, the correlation coefficient, is presented for each equation in column 3. It can be seen from this table and from Figure 6 that the equations are a fairly good fit to the hole dimension data. The relatively large spread of the prediction errors for equation (2) is due to an inherent physical uncertainty in the

TABLE 3. REGRESSION ANALYSIS OF BUMPER HOLE DIMENSION DATA, ERROR SUMMARY

	$\%\epsilon_{avg}$	σ (%)	100 R^2
D_{min}/d	0.001	6.550	72.3
D_{max}/d	0.055	11.410	86.1

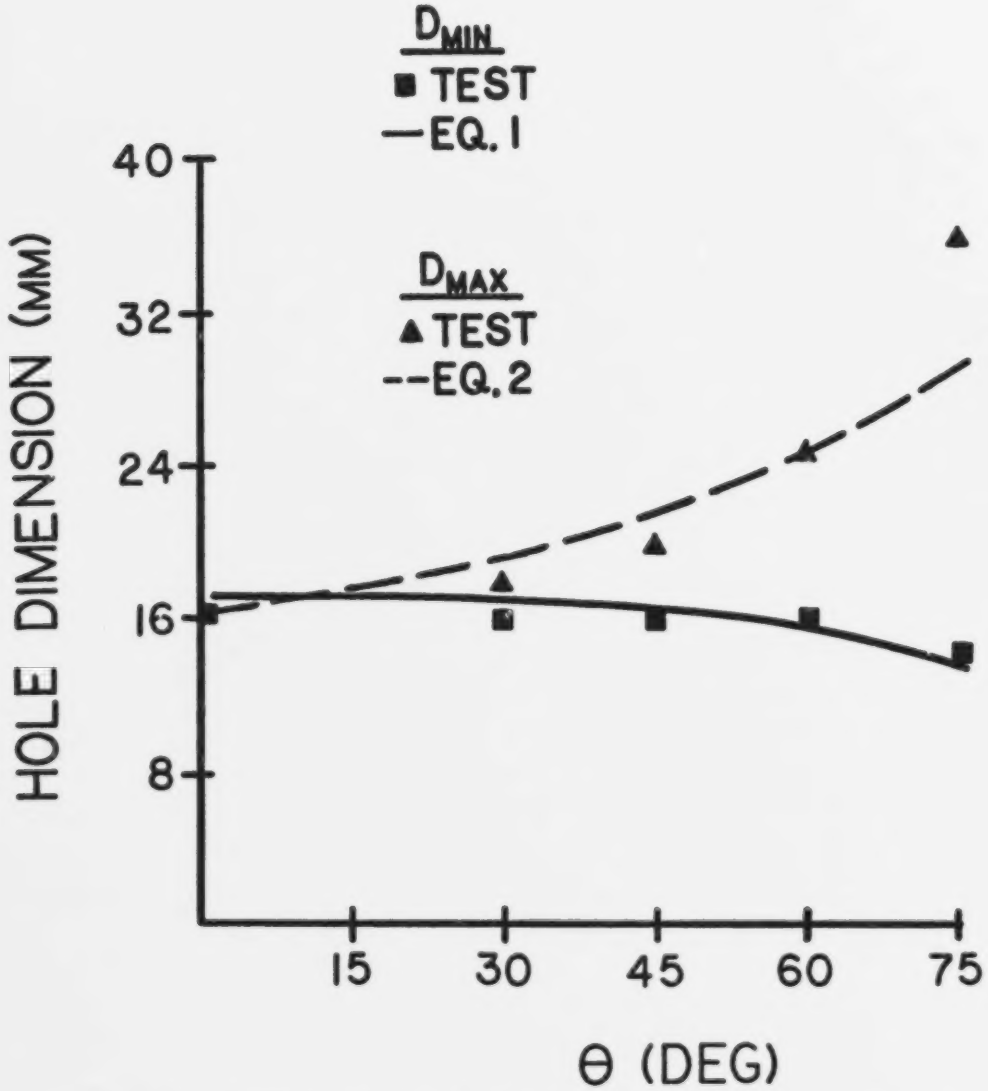

Figure 6. Bumper plate hole dimensions: Test data compared with regression equation predictions.

maximum hole dimensions, especially in holes produced by high obliquity impacts. It has been shown previously that a high obliquity impact will tear, as well as perforate, the bumper plate in the direction of the line-of-flight of the projectile [16]. The effects of this tearing process on the maximum hole dimension varied dramatically, even between similar impact test shots (note the difference in D_{max} for Tests No. 231C and 231D).

A comparison of Figure 6 with the corresponding figure in Reference 16 shows that the new equations have a much wider range of applicability and possess a higher degree of accuracy than the previously developed equations. It is noted that these equations are valid only for projectiles and plates made of the same material, for $0.0853 < t_s/d < 0.4278$, $5.0 < V < 8.0$ km/sec, and for trajectory obliquities between 0 and 75 deg.

It is also interesting to note that the coefficients and exponents of equation (1) are very similar to the corresponding constants in the equation obtained by Maiden, et al. [7] for hole diameters in thin plates under normal high speed impact. This equation is given below.

$$D/d = 2.40(V/C)\ (t_s/d)^{0.666} + 0.90 \qquad (3)$$

where D is the diameter of the (circular) hole in the bumper plate.

PENETRATION DEBRIS CENTER-OF-MASS TRAJECTORY ANALYSIS

As in the case of the hole dimension equations, the equations for θ_1 and θ_2 obtained previously were updated by including the data from the new test specimens in the regression database. Empirical expressions for θ_1 and θ_2 were obtained as functions of projectile diameter, impact velocity, and trajectory obliquity with the following results:

$$\theta_1/\theta = 0.184(V/C)^{0.290} \cos^{1.372}\theta (t_s/d)^{-0.488}, \quad 45° < \theta < 75° \qquad (4)$$

$$\theta_2/\theta = 0.490(V/C)^{-0.056} \cos^{0.909}\theta (t_s/d)^{-0.626}, \quad 30° < \theta < 75° . \qquad (5)$$

The averages and standard deviations of the prediction errors and the correlation coefficients for each equation are presented in Table 4. The spread of the prediction errors was found to be somewhat large for these equations. This is probably due to the fact that it was often difficult to determine the exact boundaries of the "normal" and "in-line" debris crater clusters and their centers of mass. The actual values of the penetration angles are therefore seen to be somewhat dependent on the person performing the analyses. However, equations (4) and (5) are a significant improvement over the corresponding equations developed in the previous study [16]. These equations are more compact, and for the most part have a higher correlation with experimental results than the equations previously developed.

TABLE 4. ANGLE DATA REGRESSION ANALYSIS, ERROR SUMMARY

	$\%\varepsilon_{avg}$	σ (%)	100 R^2
θ_1/θ	0.612	11.029	94.8
θ_2/θ	2.209	21.436	73.9
γ_1/θ	0.187	6.261	73.8
γ_2/θ	2.515	22.436	91.5
α_c/θ	0.889	13.676	85.5
α_{99}/θ	0.640	11.832	75.6

A comparison of predicted and actual values of θ_1 and θ_2 is presented in Figure 7. It is seen that the "in-line" trajectory angle, θ_2, is not a single-valued function of trajectory obliquity, θ. In fact, θ_2 varies directly with θ up to a critical value, θ_{cr}, between 60 and 65 deg and then decreases with further increases in θ. This reversal at $\theta = \theta_{cr}$ corresponds to a change in the loc tion of the most severe damage from the pressure wall plate for $\theta < \theta_{cr}$ to the ricochet witness plate for $\theta > \theta_{cr}$.

It is again noted that equations (4) and (5) are valid only for projectiles and plates of the same material, for $0.0853 < t_s/d < 0.4278$, and for $5.0 < V < 8.0$ km/sec.

PENETRATION DEBRIS CLOUD CONE ANGLES

In an effort to assess the extent of penetration damage as well as location, equations relating the spread of penetration debris were developed. These equations, together with the center of mass trajectory equations, could be used to assess whether or not the debris clouds formed as the result of an oblique impact would overlap and concentrate their energy or separate and distribute their energy upon the pressure wall plate.

Inspection of damage pressure wall plates revealed that for trajectory obliquities below 30 deg and above 65 deg there was significant overlapping of the projectile and bumper plate debris clouds. However, for intermediate obliquities, whether or not there was any separation of the debris clouds depended on the original impact parameters. It is interesting to note that in the case of low trajectory obliquity, the overlapping of the debris clouds concentrated the debris into a much smaller volume and thereby increased the damage potential of the penetrating debris particles. However, in the high obliquity regime, because so few penetration particles were created, the overlapping of the debris clouds did not contribute significantly to the damage caused by the debris particles.

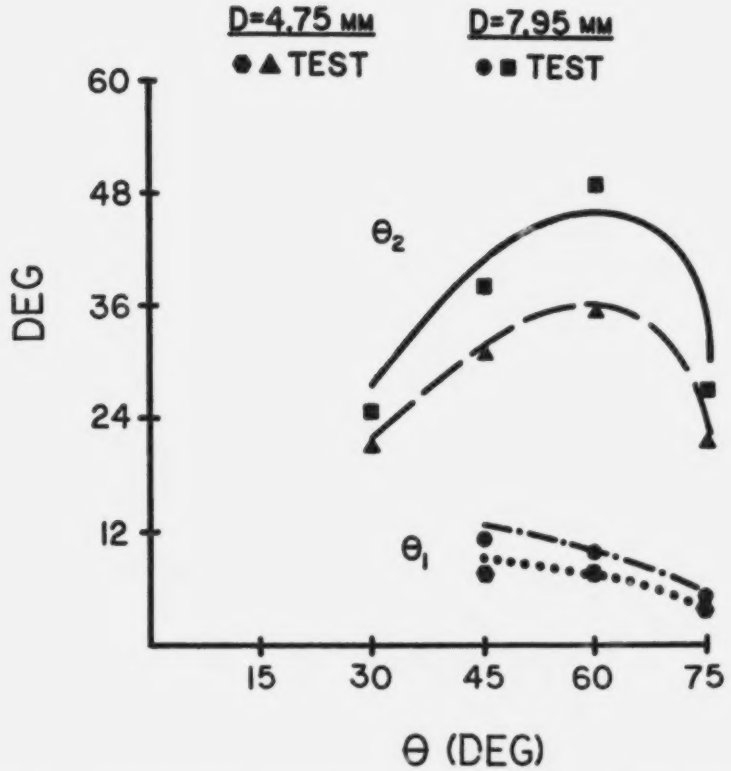

Figure 7. Penetration fragments trajectories: Test data compared with regression equation predictions.

The equations for the cone angles of the debris clouds were obtained using standard multiple linear regression techniques with the following results.

$$\gamma_1/\theta = 0.417(V/C)^{0.228} \cos^{0.225} \theta(t_s/d)^{-0.491} \quad , \quad 45° < \theta < 75° \qquad (6)$$

$$\gamma_2/\theta = 2.539(V/C)^{1.217} \cos^{2.972} \theta(t_s/d)^{0.296} \quad , \quad 30° < \theta < 65° \quad . \qquad (7)$$

It is noted that the regions of applicability of the cone angle equations are indicative of the overlapping phenomena for low and high trajectory obliquities. The averages and standard deviations of the prediction errors and the correlation coefficients for equations (6) and (7) are presented in Table 4 where it is seen that the equations are a fairly good fit to the cone angle data. Once again, these equations are valid for projectiles and plates of the same material, for $0.0853 < t_s/d < 0.4278$, and for $5.0 < V < 8.0$ km/sec.

RICOCHET ANGLE ANALYSIS

Empirical expressions for α_c and α_{99} obtained previously were updated through a regression of the expanded database with the following results.

$$\alpha_c/\theta = 0.033(V/C)^{0.982} \sin^{-3.215} \theta(t_s/d)^{-0.531} \quad , \quad 45° < \theta < 75° \qquad (8)$$

$$\alpha_{99}/\theta = 0.194(V/C)^{0.390} \sin^{-1.874} \upsilon(t_s/d)^{-0.235} \quad , \quad 45° < \theta < 75° \quad . \qquad (9)$$

Average prediction errors, standard deviations, and correlation coefficients are presented in Table 4. Although the average prediction errors are quite small, the spread of the prediction errors is also somewhat large for these equations. This is probably due to error in the regression data itself which can be attributed to several factors. First, the ricochet witness plates were finite in height, and, as a result, some ricochet debris particles escaped detection. Second, ricochet debris holes and craters were frequently observed to cluster and overlap, especially for original trajectory obliquities greater than 60 deg. In these cases it was difficult to determine the exact number of holes or craters on the ricochet witness plate.

Plots of predicted and actual ricochet angle values are presented in Figure 8. It can be seen from these curves that α_c has a weaker dependence on θ than α_{99},

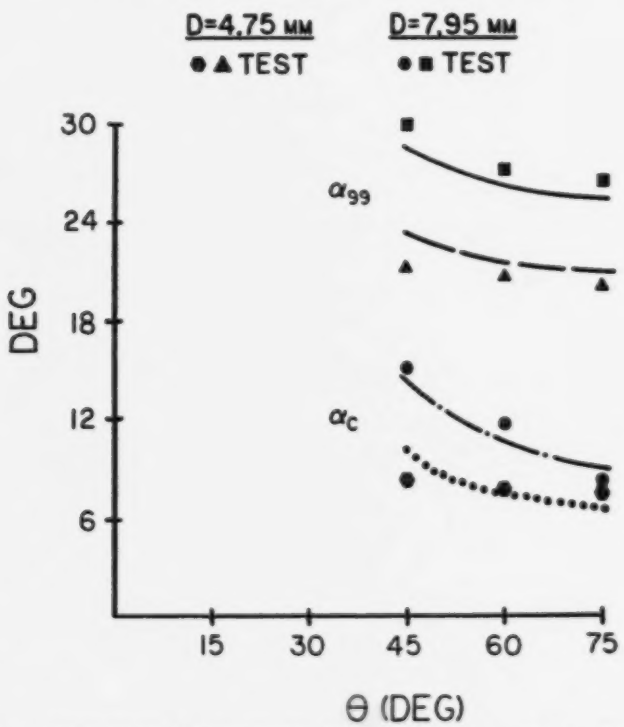

Figure 8. Ricochet fragments trajectories: Test data compared with regression equation predictions.

which decreases significantly as θ increases. This feature is indicative of the fact that the majority of the ricochet debris particles travel along trajectories that are very close to the bumper plate, regardless of the original angle of impact.

It is also noted that these equations are valid only for projectiles and plates of the same material and for $0.0853 < t_s/d < 0.4278$ and $5.0 < V < 8.0$ km/sec.

RICOCHET PARTICLE SIZE AND VELOCITY ANALYSIS

The next task in the analysis of the oblique impact test specimens was to determine the sizes and velocities of typical ricochet debris particles based on the crater damage found on ricochet witness plates. It was proposed to use equations for penetration depth in thick plates together with measured crater depths to determine, in an inverse fashion, the diameter and velocity of the debris particles that caused the craters. Visual inspection of damaged ricochet witness plates revealed several interesting features that address the validity of this method.

First, the surface openings of ricochet witness plate craters formed by debris impacts were very nearly circular, which is indicative of normal or near-normal impact trajectories. This observation is confirmed by the data in Table 1 which indicates that 99 percent of the ricochet debris impact obliquities are less than 30 deg, regardless of the original angle of impact. Second, in the tests where the ricochet witness plates were thicker than the standard 2.54 mm (0.1 in.), the reverse sides of the plates remained smooth and undamaged even though the front sides exhibited significant crater damage. In these cases, the post-impact appearance of the ricochet witness plate was identical to that of a "thick plate" subjected to the same impact loading. Based on these observations, the proposal to use thick plate equations is justified provided that the reverse side of the ricochet witness plate in which the crater depths are measured is smooth and undamaged (i.e., no spall or dimpling).

Examination of existing penetration depth equations revealed a strong coupling between particle size and velocity effects. That is, the same size crater can be produced by a small particle traveling at a high speed or by a larger particle traveling at a slower speed. In order to have a unique solution for the particle size and speed, a second set of equations describing another measurable crater quantity was needed. A search of existing literature on cratering phenomena in hypervelocity impact suggested crater volume to be such a quantity. Thus, a crater volume equation used in conjunction with an equation for penetration depth could be used to solve uniquely for particle size and speed. Since it is more facile to measure the surface diameter of an impact crater than it is to determine its exact volume, the crater volume equations were rewritten in terms of surface diameter. The analysis then proceeded as follows.

First, penetration depths and surface diameters of the three largest craters on ricochet witness plates with undamaged rear surfaces were measured. In this manner, the diameters and velocities subsequently calculated would represent upper bounds on ricochet debris sizes and speeds. Next, the equations for penetration depth and crater diameter were paired. Each pair of equations was then solved for particle diameter and velocity in terms of all other parameters, such as density, yield strength, wave speed, etc. Substitution of the appropriate values for these parameters in these equations yielded an estimate for the size and speed of the particle that produced a particular crater. This calculation was performed for each crater using 12 penetration depth equations and 6 crater diameter equations. These equations,

some rewritten for consistency, are listed in the Appendix. Theoretically, this should have resulted in 72 estimates for the diameter and 72 estimates for the velocity of each crater producing projectile.

However, in the process of pairing the penetration depth and crater diameter equations, it became evident that not all equation pairs were compatible. Due to the exponential form of the equations, certain combinations of equations led to powers of zero for an unknown diameter or velocity. These particular equation pairs, therefore, could not be used to solve for the unknown quantities. This situation is analogous to finding the intersection of two parallel lines in Euclidean geometry.

Furthermore, even though an equation pair did produce a solution, the resultant particle size occasionally exceeded that of the crater diameter, sometimes by a factor of three or four. However, it was previously shown that the heated material surrounding a high speed impact crater relaxes as it cools after the impact event. This causes a reduction in crater diameter and depth of approximately 20 to 25 percent [24,25]. Therefore, it is indeed conceivable that a crater could have been produced by a particle whose diameter exceeded the size of the surface opening, but it is unlikely that the particle diameter could have exceeded the surface diameter by more than 25 percent. As a result, particle diameter values greater than 1.25 times the crater surface diameter were rejected. These two considerations reduced the number of calculated values from 72 to approximately 25. The averages of the acceptable diameters and velocities for each particle were then assumed to be valid estimates of its actual diameter and speed.

Measured crater depths and surface diameters for appropriate impact tests are provided in Table 5. The resulting estimated particle diameters and velocities corresponding to these depths and diameters are presented in Table 6. The average values of these diameters and velocities (plus and minus a standard deviation) are shown in Table 7 as functions of original projectile diameter and impact velocity. Lastly, using the penetration depth and crater diameter equations, the estimated particle diameters and speeds are used to calculate the depth of penetration and surface diameter of a crater that would form if such a particle were to strike a ricochet witness plate of the same material. The percent differences between the actual crater depths and surface diameters in Table 5 and those calculated using the equations in the Appendix and the corresponding particle diameters and impact velocities are shown in Table 8. An examination of the tables reveals several interesting points.

First, from Tables 6 and 7, high obliquity impacts and impacts by large projectiles produce larger ricochet debris particles than impacts at low obliquities or impacts by small projectiles. This is a quantitative verification of the qualitative statement that the severity of the ricochet damage is directly related to the trajectory obliquity and size of the original projectile [16]. The average diameter of the ricochet debris particles is calculated to be approximately 40 percent of the parent projectile diameter, which corresponds to a fractional volume of approximately 6.4 percent. However, average ricochet debris particle velocity does not seem to vary significantly with respect to impact obliquity and speed and can vary between 24 and 36 percent of the original projectile impact velocity.

Second, from the prediction errors in Table 8, particle diameters and speeds calculated using this technique will probably yield surface diameters fairly close to the actual values, but will over-estimate penetration depths by an average of approximately 20 percent. However, since the average pentration depth error is

TABLE 5. MEASURED PENETRATION DEPTHS AND CRATER DIAMETERS

Impact Parameters				Penetration Depths and Diameters					
Test Number	Velocity km/sec	θ deg	d cm	P_1 cm	d_{h1} cm	P_2 cm	d_{h2} cm	P_3 cm	d_{h3} cm
EHAB	6.91	75	0.795	0.615	0.734	0.368	0.686	0.483	0.566
EHBP	7.22	75	0.635	0.495	0.650	0.361	0.602	0.310	0.445
EHCP	7.58	75	0.475	0.386	0.599	0.318	0.447	0.345	0.422
EHRP2	6.80	65	0.795	0.371	0.632	0.229	0.445	0.211	0.445
EHRP5	7.51	65	0.635	0.305	0.528	0.330	0.546	0.203	0.411
EHRP1	6.87	60	0.795	0.140	0.254	0.094	0.241	0.117	0.244
EHRP4	7.65	60	0.635	0.152	0.279	0.216	0.371	0.157	0.328
EHRP7	7.98	60	0.475	0.323	0.488	0.254	0.396	0.203	0.465
EHRP3	6.78	45	0.795	0.165	0.368	0.150	0.320	0.135	0.343
EHRP6	7.57	45	0.635	0.097	0.201	0.114	0.267	0.084	0.211
EHRP8	7.34	45	0.475	0.155	0.262	0.137	0.279	0.168	0.295

TABLE 6. CALCULATED PARTICLE DIAMETERS AND VELOCITIES

Impact Parameters				Particle Diameters and Velocities					
Test Number	Velocity km/sec	θ deg	d cm	d_1 cm	V_1 km/sec	d_2 cm	V_2 km/sec	d_3 cm	V_3 km/sec
EHAB	6.91	75	0.795	0.472	2.40	0.452	1.97	0.346	2.45
EHBP	7.22	75	0.635	0.389	2.58	0.395	2.06	0.254	2.50
EHCP	7.58	75	0.475	0.390	2.20	0.253	2.55	0.261	2.47
EHRP2	6.80	65	0.795	0.350	1.96	0.361	2.03	0.243	1.99
EHRP5	7.51	65	0.635	0.302	2.28	0.253	2.25	0.289	1.80
EHRP1	6.87	60	0.795	0.413	1.98	0.289	1.85	0.260	2.21
EHRP4	7.65	60	0.635	0.176	2.08	0.240	2.02	0.208	2.01
EHRP7	7.98	60	0.475	0.125	2.06	0.157	1.97	0.123	1.95
EHRP3	6.78	45	0.795	0.160	2.09	0.140	1.93	0.148	2.19
EHRP6	7.57	45	0.635	0.224	1.98	0.183	2.24	0.191	1.97
EHRP8	7.34	45	0.475	0.169	2.07	0.168	2.13	0.186	2.09

TABLE 7. AVERAGE RICOCHET PARTICLE DIAMETERS AND VELOCITIES AS A FUNCTION OF ORIGINAL PROJECTILE OBLIQUITY AND DIAMETER (cm) (Original Impact Velocity 6.7 < V < 8.0 km/sec)

		d_{avg} (cm)	V_{avg} (km/sec)
(a)	45°	0.174±0.024	2.07±0.10
	60°	0.221±0.087	2.01±0.09
	65°	0.299±0.044	2.05±0.17
	75°	0.357±0.079	2.35±0.21
(b)	0.475	0.203±0.080	2.17±0.20
	0.635	0.258±0.070	2.15±0.19
	0.795	0.303±0.110	2.08±0.18

TABLE 8. PREDICTION ERRORS USING CALCULATED PARTICLE DIAMETERS AND VELOCITIES

Impact Parameters				Prediction Errors (%)					
Test Number	Velocity km/sec	θ deg	d cm	P_1	d_{h1}	P_2	d_{h2}	P_3	d_{h3}
EHAB	6.91	75	0.795	-6.0	16.7	28.0	5.4	-10.9	12.7
EHBP	7.22	75	0.635	1.8	13.8	17.9	7.8	3.0	6.8
EHCP	7.58	75	0.475	15.1	11.9	1.7	7.1	-6.2	14.6
EHRP2	6.80	65	0.795	19.0	6.2	16.3	7.7	24.2	-13.7
EHRP5	7.51	65	0.635	9.3	9.0	14.5	11.3	43.3	-14.8
EHRP1	6.87	60	0.795	16.5	4.8	24.1	-0.4	39.5	-8.7
EHRP4	7.65	60	0.635	24.1	4.5	17.4	5.4	38.5	-6.4
EHRP7	7.98	60	0.475	37.0	-7.0	40.2	-14.2	47.7	-16.1
EHRP3	6.78	45	0.795	23.1	4.6	50.1	-16.6	41.2	-5.6
EHRP6	7.57	45	0.635	40.2	-11.5	39.1	-9.8	45.4	-19.2
EHRP8	7.34	45	0.475	16.5	6.6	33.6	-8.3	19.6	4.9

positive, the error is on the side of safety. The larger penetration depth prediction error due to the fact that the penetration depth equations used in this study often differ from each other by as much as 30 percent in their prediction of penetration depth. Predictions of crater diameter, however, more closely approximated the actual values due to the fact that the crater diameter equations generally yielded values that were within 5 to 10 percent of each other.

DESIGN OF EXTERNAL DEBRIS CONTAINMENT SHIELDS

Development of Shield Concept

It has been shown that an obliquely incident hypervelocity projectile will produce ricochet debris particles that can severely damage external flight critical systems of a spacecraft. For the test parameters considered, average particles were found to be as large as 0.25 cm (0.1 in.) and travel as fast as 2.1 km/sec (6,890 ft/sec). It is evident that in the event of an on-orbit impact the ricochet debris that is produced must be contained in order to guarantee the safety of the mission and to avoid jeopardizing the safety of future missions into the same environment.

Although the concepts and procedures developed in the following sections are applicable to any type of spacecraft geometry and orientation, for the purposes of this investigation it is assumed that the spacecraft for which containment shielding is to be designed is cylindrical and is oriented such that its velocity vector is perpendicular to its longitudinal axis. For the International Space Station, this implies that the modules are configured as shown in Figure 9 (illustration courtesy of Boeing Aerospace Corporation [15]). In this figure, the shaded areas are those which are most likely to be impacted by orbital debris.

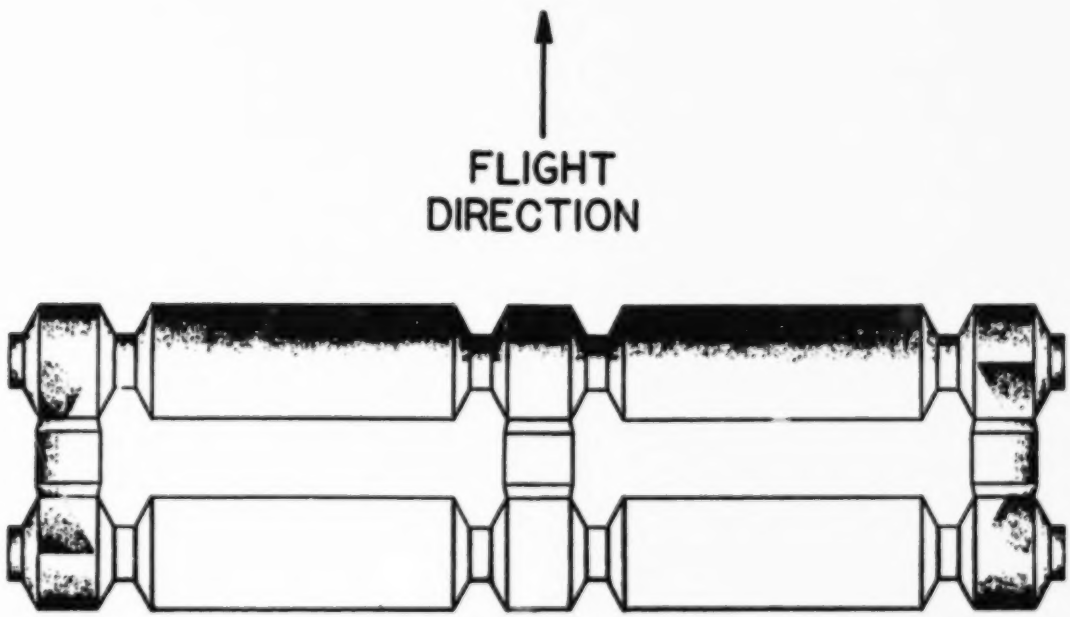

Figure 9. Space station module orientation.

A cross-section of a typical module is given in Figure 10, showing only the module wall, bumper plate, and an array of containment shield elements. A V-shaped arrangement of two rectangular panels was chosen as the basic shield element configuration due to its ability to contain ricochet debris that would be produced by impacts with an equal probability of occurring "above" or "below" the flight direction vector. In the assumed module orientation, shield elements would run parallel to the longitudinal axis of the module and would be evenly spaced along the circumference of the exposed portion of the module. It is interesting to note that in such a design, each panel of the shield element will serve as a bumper for the other panel and will trap any secondary "penetration" debris that may form as a result of a ricochet debris particle impact.

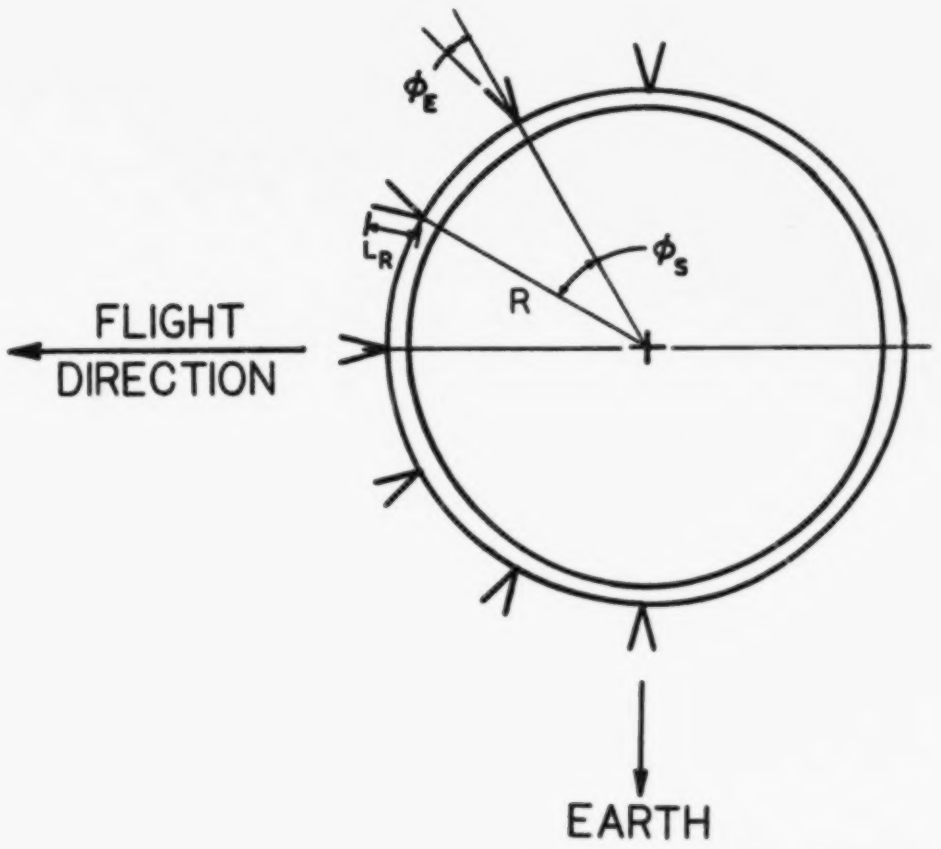

Figure 10. Space station module cross-section with containment shield parameters.

In the design of such a containment shield system, it is assumed that the radius R of the spacecraft is a known quantity. The unknown quantities that need to be determined are the element panel length l_r, panel thickness t_p, panel inclination ϕ_e, and the element separation ϕ_s. Acceptable design values for these parameters are limited by the following phenomenological considerations.

1) The most dangerous ricochet debris particles are formed by impacts whose trajectory obliquities are greater than 60 deg. Therefore, it is required that the angular separation of the containment shield elements be such that any projectile impacting the spacecraft between two adjacent shield elements have a trajectory obliquity of no more than 60 deg (Design Condition No. 1).

2) Low obliquity impacts produce ricochet debris particles that can travel along trajectories of 30 deg with respect to the plane of the bumper plate. These trajectory obliquities decrease as the obliquity of the parent projectile increases. Therefore, it is required that the length l_r of each containment shield element panel be sufficient to trap ricochet debris formed from an impact with a low trajectory obliquity, i.e., less than 45 deg (Design Condition No. 2).

The design procedure will basically consist of selecting a panel length, panel inclination, and an element separation and then ensuring that the chosen values satisfy Design Conditions No. 1 and No. 2. Panel thickness is calculated using a technique currently employed in the design of dual-wall structures.

Design Equations

Consider a projectile about to strike the external bumper wall of a cylindrical spacecraft with radius R (Fig. 11). In the following paragraphs, the terms "downstream" and "upstream" refer respectively to the shield elements in front of and behind an actual or projected impact site. Let ϕ_m be the angular separation between the site of impact and a "downstream" shielding element, γ the obliquity of its trajectory with respect to the outward normal of the spacecraft hull, and let γ_{max} be the maximum value of all such obliquities. The maximum obliquity occurs when the trajectory of an incoming projectile grazes and "upstream" shield element and terminates at the base of an adjacent "downstream" element. Thus, when $\gamma = \gamma_{max}$, then $\phi_m = 0$.

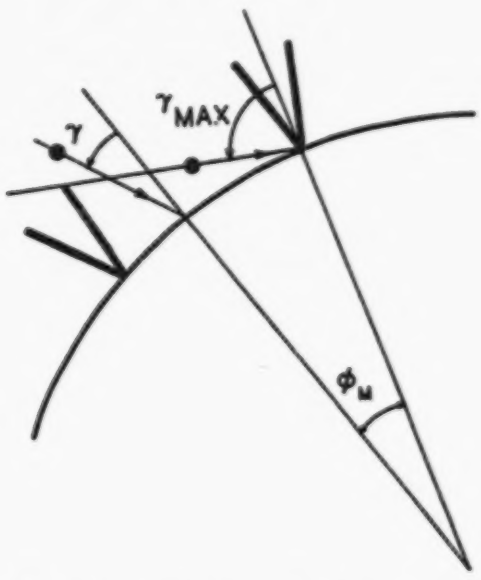

Figure 11. Meteoroid/space debris trajectories.

According to Design Condition No. 1, the shield elements must be spaced so that all trajectory obliquities are less than 60 deg. In Figure 12, a projectile traveling along a trajectory with an obliquity γ grazes the outermost point D of shield element panel DE and impacts at point A; point C lies at the foot of the perpendicular drawn from point D to the extension of radius EF; point B is the foot of the perpendicular from point C to the extension of radius AB. Then angle CFB = $\phi_s - \phi_m$, angle CED = ϕ_e, and angle DAB = γ. Let angle ECA = α, angle CDA = ε, and angle CAB = γ_o; then angle CAD = $\gamma_o - \gamma$. Lastly, let CA = z, DA = u, CE = v, CB = y, and BA = x.

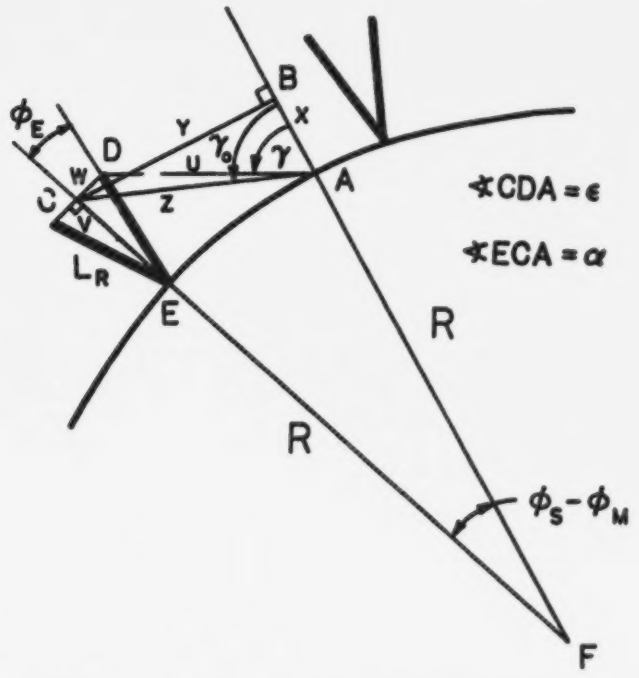

Figure 12. Containment shield geometry for Design Condition No. 1.

In triangle FBC,

$$\frac{R + x}{R + l_r \cos \phi_e} = \cos (\phi_s - \phi_m)$$

from which

$$x = (R + l_r \cos \phi_e) \cos (\phi_s - \phi_m) - R \qquad (10)$$

Also,

$$\frac{y}{R + l_r \cos \phi_e} = \sin (\phi_s - \phi_m)$$

from which

$$y = (R + l_r \cos \phi_e) \sin (\phi_s - \phi_m) \quad . \tag{11}$$

And,

$$\gamma_o = \tan^{-1} (y/x) \quad , \tag{12}$$

$$z = (x^2 + y^2)^{1/2} \quad . \tag{13}$$

In triangle DCE,

$$w = l_r \sin \phi_e \quad , \tag{14a}$$

$$v = l_r \cos \phi_e \quad . \tag{14b}$$

Applying the Law of Cosines to triangle DCA,

$$w^2 = u^2 + z^2 - 2uz \cos (\gamma_o - \gamma) \quad . \tag{15}$$

Applying the Law of Sines to triangle CAD,

$$\frac{z}{\sin \varepsilon} = \frac{u}{\sin (90 - \alpha)} \quad . \tag{16}$$

In triangle ACF,

$$\alpha + \phi_s - \phi_m + 180 - \gamma_o = 180$$

from which

$$\alpha = \gamma_o - (\phi_s - \phi_m) \quad . \tag{17}$$

In triangle CAD,

$$\varepsilon + 90 - \alpha + \gamma_o - \gamma = 180$$

from which

$$\varepsilon = 90 + \gamma - (\phi_s - \phi_m) \quad . \tag{18}$$

Substituting equations (17) and (18) into equation (16), noting that sin (90 ± β) = cos β, and rearranging yields

$$u = gz \quad , \tag{19}$$

where

$$g = \cos [\gamma_o - (\phi_s - \phi_m)]/\cos [\gamma - (\phi_s - \phi_m)] \quad . \tag{20}$$

Substituting equation (19) into equation (15) and combining equations (14a) and (15) yields

$$w^2 = g^2 z^2 + z^2 - 2 gz^2 \cos (\gamma_o - \gamma) = l_r^2 \sin^2 \phi_e \quad . \tag{21}$$

Substituting for z according to equation (13) and rewriting equation (21) as an equation in terms of the variable g yields

$$g^2 - 2 g \cos (\gamma_o - \gamma) - l_r^2 \sin^2 \phi_e/(x^2 + y^2) + 1 = 0 \quad . \tag{22}$$

Substituting for x and y according to equations (10) and (11), respectively, yields the equation

$$g^2 - 2 g \cos (\gamma_o - \gamma) + 1 - l_r^2 \sin^2 \phi_e/[R^2 + (R + l_r \cos \phi_e)^2$$

$$- 2R (R + l_r \cos \phi_e) \cos (\phi_s - \phi_m)] = 0 \tag{23}$$

where $g(\gamma, \gamma_o, \phi_s, \phi_m)$ is given by equation (20) and

$$\gamma_o = \tan^{-1} \{(R + l_r \cos \phi_e) \sin (\phi_s - \phi_m) / (l_r \cos \phi_e - (R + l_r \cos \phi_e) [1 - \cos (\phi_s - \phi_m)]\} \quad . \tag{24}$$

From Figure 11, $\gamma = \gamma_{max}$ when $\phi_m = 0$. To calculate γ_{max}, set $\phi_m = 0$ in equation (23) and solve for γ. If $\gamma = \gamma_{max} < 60$ deg for the chosen values of l_r and ϕ_e, then Design Condition No. 1 is satisfied.

According to Design Condition No. 2, shield element panels must be long enough to contain ricochet debris formed by low obliquity impacts. Panel length varies directly with the distance from the impact site to the foot of the panel. Maximum panel length will be achieved by considering a low obliquity impact trajectory that grazes the outermost point of an "upstream" element panel and places the impact site as far away as possible from the adjacent "downstream" element.

In Figure 13, point A is the point of impact on the bumper of a projectile traveling along such a trajectory; BD is the "downstream" shield element panel that must be long enough to contain the ricochet debris within angle BAD; point C lies at the intersection of line AD and the extension of radius BF; point G is a point on the line tangent to the circle at point A; point H is a point on the extension of

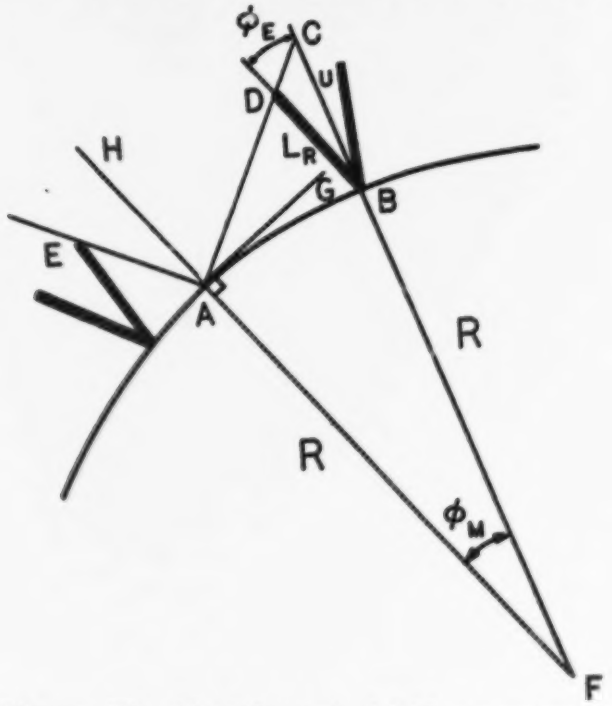

Figure 13. Containment shield geometry for Design Condition No. 2.

radius AF. Then angle AFC = ϕ_m, angle CBD = ϕ_e, angle CAG = 30 deg, angle CAF = 120 deg, angle ACF = 60 - ϕ_m, AF = BF = R, and BD = l_r. Let the trajectory obliquity (angle EAH) and the ricochet cone angle DAG both be equal to 30 deg, and let CB = u.

Applying the Law of Sines to triangle CAF yields

$$\frac{u + R}{\sin 120} = \frac{R}{\sin (60 - \phi_m)} \quad . \tag{25}$$

Solving for u yields

$$u = R\,[1 - (\cos \phi_m - 0.577 \sin \phi_m)]/(\cos \phi_m - 0.577 \sin \phi_m) \quad . \tag{26}$$

Applying the Law of Sines to triangle CBD yields

$$\frac{u}{\sin (120 + \phi_m - \phi_e)} = \frac{l_r}{\sin (60 - \phi_m)} \quad . \tag{27}$$

Solving for l_r yields

$$l_r = R\,[1 - f(\phi_m, 0)]/f(\phi_m, \phi_e) \tag{28}$$

where

$$f(x,y) = \cos (x - y) - 0.577 \sin (x - y) \quad . \tag{29}$$

Thus, if the value of l_r for the "downstream" panel calculated using equation (28) is less than the assumed value of l_r, then the assumed panel length is sufficient and Design Condition No. 2 is satisfied.

Panel thicknesses can be calculated using a modified form of the following equation for rear-sheet thickness of a dual-wall structure [26].

$$t_2/d = 5.08\, V^{0.278}\, (t_1/d)^{-0.528}\, (h/d)^{-1.39} \tag{30}$$

where t_1 and t_2 are the thicknesses of the first and second sheets, respectively, and h is the separation between the two sheets. Since the two panels are not uniformly

spaced, an equivalent "separation distance" was calculated as follows. Based on previous examinations of damaged ricochet witness plates, it was assumed that the majority of ricochet particle impacts will occur within a distance of $l_r/2$ away from the base of the shield element. Using the relationship between arc length, angle, and radius, the separation distance was approximated by the following equation.

$$h \sim (l_r/2)\ (2\phi_e) = l_r\ \phi_e \quad . \tag{31}$$

In order to equally protect against impacts above and below the flight direction vector, the element design is assumed to be symmetric with respect to the outward normal of the spacecraft. Therefore, letting $t_1 = t_2 = t_p$, substituting for h in equation (30) according to equation (31) and solving for t_p yields the following expression for panel thickness.

$$t_p/d = 2.897\ V^{0.182}\ (l_r\phi_e/d)^{-0.910} \quad . \tag{32}$$

Design Procedure

The procedure to be used for the design containment shielding panels is as follows:

Step No. 1: Input assumed values for ϕ_s, ϕ_e, l_r, and R. Based on previous experience, satisfactory initial values for these parameters are ϕ_s = 10 deg, ϕ_e = 5 deg, and l_r = 0.1R to 0.2R.

Step No. 2: Calculate γ_{max} using equation (23) with $\phi_m = 0$. Is $\gamma_{max} < 60$ deg? If yes, proceed to Step No. 3; if no, choose a smaller ϕ_s or a larger l_r and repeat this step.

Step No. 3: Calculate ϕ_m for the assumed values of ϕ_s, ϕ_e, and l_r using equation (23) with γ = 30 deg.

Step No. 4: Calculate the length l_r of the "downstream" shielding element panel using equation (28). Is the assumed length l_r greater than the "downstream" length l_r? If yes, proceed to Step No. 5; if no, choose a larger l_r or a smaller ϕ_s and go to Step No. 2.

Step No. 5: The values of ϕ_s, ϕ_e, and l_r are acceptable. Calculate t_p using equation (32).

Several examples of panel design using this procedure and the accompanying equations are presented in the next section.

Examples

A matrix of acceptable design values for ϕ_s, ϕ_e, l_r, and t_p is given in Table 9. Panel length values were obtained for a spacecraft radius of 2.235 m (7 ft. 4 in.); thickness values were obtained using the average upper bound values for ricochet particle diameter and speed, namely, d = 0.25 cm and V = 2.1 km/sec.

TABLE 9. PANEL LENGTH (cm) AND THICKNESS (cm) AS A FUNCTION OF PANEL INCLINATION AND SHIELD ELEMENT SEPARATION

	Panel Inclination (ϕ_e)							
	5°		10°		15°		20°	
ϕ_s (deg)	l_r	t_p	l_r	t_p	l_r	t_p	l_r	t_p
5	12.19	0.222	11.58	0.124	10.97	0.090	10.67	0.071
10	27.43	0.106	25.91	0.060	24.38	0.044	23.47	0.035
15	48.77	0.063	44.20	0.037	42.67	0.026	38.10	0.023
20	73.15	0.043	67.06	0.025	60.96	0.019	56.39	0.016

It can be seen in Table 9 that a small change in ϕ_e produces only a minor change in l_r whereas a similar small change in ϕ_s results in a major change in l_r. However, panel thickness is seen to be strongly dependent on the angle of inclination as well as the separation angle.

CONCLUSIONS AND RECOMMENDATIONS

This section consists of conclusions formulated during the course of this study together with a summary of those presented in the previous investigation [16]. These observations must be considered in the design of spacecraft meteoroid and space debris protection systems.

There exists a critical angle of obliquity. Projectiles with angles of obliquity less than this critical angle produce significant damage to the pressure wall plate and little damage to the ricochet witness plate in a hypervelocity impact test specimen. However, the damage produced on the pressure wall plate by projectiles with trajectory obliquities greater than the critical angle is minimal compared to the damage sustained by the ricochet witness plate. This critical angle is estimated to have a value between 60 and 65 deg.

Low obliquity hypervelocity impacts are potentially more dangerous to a pressurized spacecraft module than normal impacts with otherwise identical parameters. In a low obliquity impact, the penetration debris cloud is more concentrated than in a normal impact. Even a small obliquity will concentrate the kinetic energies of the penetration debris particles which in turn can cause penetration of the pressure wall.

High obliquity impact penetration debris clouds have a lower damage potential than low obliquity impact debris clouds for two reasons. First, the quantity of penetration debris in high obliquity impacts is much lower than the quantity of penetration debris in low obliquity impacts. Second, the bumper plate debris and projectile debris clouds separate in a high obliquity impact which serves to dissipate the kinetic energy of the debris particles. Empirical equations that can be used to estimate the location and the extent of penetration damage were developed based on penetration angle data. These equations can also be used to determine whether or not the bumper plate and projectile debris clouds will overlap and combine their penetrating potentials or separate and dissipate their kinetic energies.

However, high obliquity impacts have a very high potential for damage to external spacecraft systems because of the large volume of ricochet debris particles that they produce. The most serious ricochet debris damage was found to occur within an angle of 15 deg with respect to the plane of the bumper plate, regardless of the original angle of impact. For trajectory obliquities greater than 60 deg, the ricochet witness plate was completely perforated at the bumper plate/ricochet witness plate boundary. A set of empirical equations that predict the farthest ricochet debris particle trajectory and the trajectory of the center of mass of the ricochet debris particle cloud were developed based on ricochet angle data.

An analysis of ricochet witness plate crater damage revealed that an average ricochet debris particle diameter can be as large as 40 percent of the parent projectile diameter and can travel at a speed of up to 36 percent of the original impact velocity. It is imperative that the issue of ricochet debris particle damage to external spacecraft systems be addressed in the development of spacecraft destined for the meteoroid or space debris environment.

A design concept for an external ricochet debris containment panel system was developed. Panel dimensions were found to be strongly dependent on the spatial distribution of containment shield elements around an exposed portion of a spacecraft and the inclination of the panels with respect to an outwardly pointing normal.

Additional analytical and experimental investigations of oblique hypervelocity impact phenomena are strongly recommended. Additional analytical investigations would achieve several goals. First, they would provide verification of the empirical equations developed in this study. Second, they would provide reliable means of predicting ricochet damage through accurate estimates of ricochet particle sizes and velocities. Third, they would yield damage criteria that would be applicable in a variety of impact situations. Future experimental investigations using projectiles and plates from different or composite materials would better simulate on-orbit impacts of space debris and would also serve to improve and extend the applicability of current empirical equations.

REFERENCES

1. Whipple, E. L.: Meteorites and Space Travel. Astron. Journal, Vol. 52, 1947, p. 5.

2. Burch, G. T.: Multi-plate Damage Study. AF-ATL-TR-67-116, Air Force Armament Library, Elgin Air Force Base, Florida, 1967.

3. D'Anna, P. J.: A Combined System Concept For Control of the Meteoroid Hazard to Space Vehicles. J. Spacecraft, Vol. 2, No. 1, 1965, p. 33.

4. Lundeberg, J. F., Lee, D. H., and Bruch, G. T.: Impact Penetration of Manned Spacecraft. J. Spacecraft, Vol. 3, No. 2, 1966, p. 182.

5. Lundeberg, J. F., Stern, P. H., and Bristow, R. J.: Meteoroid Protection for Spacecraft Structures. NASA CR 54201, Washington, D.C., 1968.

6. McMillan, A. R.: Experimental Investigations of Simulated Meteoroid Damage to Various Spacecraft Structures. NASA CR 915, Washington, D.C., 1968.

7. Maiden, C. J., Gehring, J. W., and McMillan, A. R.: Investigation of Fundamental Mechanism of Damage to Thin Targets by Hypervelocity Projectiles. GM-DRL-TR-63-225, General Motors Defense Research Laboratory, Santa Barbara, California, 1963.

8. Maiden, C. J., and McMillan, A. R.: An Investigation of the Protection Afforded a Spacecraft by a Thin Shield. AIAA Journal, Vol. 2, No. 11, 1964, p. 1992.

9. Merzhievskii, L., and Urushkin, V.: Oblique Collision of a High-Speed Particle with a Shield. Combust., Explos., and Shock Waves, Vo. 16, No. 5, 1981, p. 551 (translation).

10. Nysmith, C. R.: Penetration Resistance of Double Sheet Structures at Velocities to 8.8 km/sec. NASA TN D-4568, Washington, D.C., 1968.

11. Riney, T. D., and Halda, E. J.: Effectiveness of Meteoroid Bumpers Composed of Two Layers of Distinct Materials. AIAA Journal, Vol. 6, No. 2, 1968, p. 338.

12. Swift, H. F., Bamford, R., and Chen, R.: Designing Space Vehicle Shields for Meteoroid Protection: A New Analysis. Adv. Space Res., Vol. 2, No. 12, 1983, p. 219.

13. Wallace, R. R., Vinson, J. R., and Kornhauser, M.: Effects of Hypervelocity Particles on Shielded Structures. ARS Journal, 1962, p. 1231.

14. Wilkinson, J. P. D.: A Penetration Criterion for Double-Walled Structures Subject to Meteoroid Impact. AIAA Journal, Vol. 7, No. 10, 1968, p. 1937.

15. Coronado, A. R., Gibbins, M. N., Wright, M. A., and Stern, P. H.: Space Station Integrated Wall Design and Penetration Damage Control. Report No. D180-30550-1, Contract NAS8-36426, Boeing Aerospace Company, Seattle, Washington, 1987.

16. Schonberg, W. P., Taylor, R. A., and Horn, R. A.: An Analysis of Penetration and Ricochet Phenomena in Oblique Hypervelocity Impact. NASA TM-100319, Washington, D.C., 1988.

17. Johnson, W. E.: Oblique Impact Calculations Using a 3-D Eulerian Code. Proceedings of the AIAA Hypervelocity Impact Symposium, AIAA Paper No. 69-353, 1969.

18. Summers, J. L.: Investigation of High Speed Impact: Regions of Impact and Impact at Oblique Angles. NASA TN D-94, Washington, D.C., 1959.

19. Taylor, R. A.: A Space Debris Simulation Facility for Spacecraft Materials Evaluation. SAMPE Quarterly, Vol. 18, No. 2, 1987, p. 28.

20. Kessler, D. J.: Orbital Environment for Space Station. Johnson Space Center Report JSC20001.

21. Schonberg, W. P., and Taylor, R. A.: Analysis of Oblique Hypervelocity Impact Phenomena. Proceedings of the 29th AIAA/ASME/ASCE/AHS SDM Conference, AIAA Paper No. 88-2370, 1988.

22. Schonberg, W. P., and Taylor, R. A.: Analysis of Oblique Hypervelocity Impact Phenomena for Meteoroid/Space Debris Protection System Design. Proceedings of the AIAA SDM Issues of the International Space Station Symposium, AIAA Paper No. 88-2463, 1988.

23. Cour-Palais, B. G.: Space Vehicle Meteoroid Shielding Design. Proceedings of the Comet Halley Micrometeoroid Hazard Workshop, ESA SP-153, 1979, p. 85.

24. Rolsten, R. F., and Hunt, H. H.: Impact Force and Crater Surface Area. AIAA J., Vol. 1, No. 8, 1963, p. 1893.

25. Rolsten, R. F., and Hunt, H. H.: Impact Force pre Crater Area Related to Tensile Strength. J. Spacecraft, Vol. 1, No. 3, 1964, p. 351.

26. Nysmith, C. R.: An Experimental Impact Investigation of Aluminum Double-Sheet Structures. Proceedings of the AIAA Hypervelocity Impact Conference, AIAA Paper No. 69-375, 1969.

27. Sawle, D. R.: Hypervelocity Impact in Thin Sheets and Semi-Infinite Targets at 15 km/sec. AIAA J., Vol. 8, No. 7, 1970, p. 1240.

28. Bruce, E. P.: Review and Analysis of High Velocity Impact Data. Proceedings of the Fifth Hypervelocity Impact Symposium, 1962, p. 439.

29. Bruce, E.: Velocity Dependence of Some Impact Phenomena. Proceedings of the Comet Halley Micrometeoroid Hazard Workshop, ESA SP-153, 1979, p. 101.

30. Goodman, E. H., and Liles, C. D.: Particle-Solid Impact Phenomena. Proceedings of the Sixth Hypervelocity Impact Symposium, 1963, p. 543.

31. Dunn, W. P.: On Material Strengths of the Hypervelocity Impact Problem. AIAA Journal, Vol. 4, No. 3, 1966, p. 535.

32. Sedgwick, R. T., Hageman, L. J., Herrmann, R. G., and Waddell, J. L.: Numerical Investigations in Penetration Mechanics. Int. J. Engng. Sci., Vol. 16, 1978, p. 859.

33. Christman, D. R.: Target Strength and Hypervelocity Impact. AIAA Journal, Vol. 4, No. 10, 1966, p. 1872.

34. Summers, J. L., and Charters, A. C.: High-Speed Impact of Metal Projectiles in Targets of Various Materials. Proceedings of the Third Hypervelocity Impact Symposium, 1959, p. 101.

35. Sorenson, N. R.: Systematic Investigation of Crater Formation in Metals. Proceedings of the Fifth Hypervelocity Impact Symposium, 1962, p. 281.

36. Herrmann, W., and Jones, A. H.: Correlation of Hypervelocity Impact Data. Proceedings of the Fifth Hypervelocity Impact Symposium, 1962, p. 389.

37. Cour-Palais, B. G.: Hypervelocity Impact Investigations and Meteoroid Shielding Experience Related to Apollo and Skylab. Orbital Debris, NASA CP-2360, 1982, p. 247.

APPENDIX

Penetration Depth Equations

Reference No. 27:

$$p/d = 2.28\ (\rho_p/\rho_t)^{2/3}\ (V/C)^{2/3}\ , \qquad V < 9\ \text{km/sec} \qquad \text{(P-1)}$$

Reference No. 28:

$$p/d = 1.96\ (\rho_p/\rho_t)^{1/2}\ (V/C)^{2/3}\ , \qquad V < 6\ \text{km/sec} \qquad \text{(P-2)}$$

Reference No. 29:

$$p/d = 1.5\ (\rho_p/\rho_t)^{1/3}\ (\rho_p V^2/2S_t)^{1/3}\ , \qquad V < 8\ \text{km/sec} \qquad \text{(P-3)}$$

Reference No. 30:

$$p/d = 2.35\ (\rho_p/\rho_t)^{0.70}\ (V/C)^{2/3}\ , \qquad V < 9\ \text{km/sec} \qquad \text{(P-4)}$$

Reference No. 31:

$$p/d = 0.63\ (\rho_p V^2/\sigma_{yt})^{1/3}\ , \qquad V < 7\ \text{km/sec} \qquad \text{(P-5)}$$

Reference No. 32:

$$p/d = 0.482\ (\rho_p/\rho_t)^{0.537}\ (V/C)^{0.576}\ (Y_t/\rho_t C^2)^{-0.235} \qquad V < 21\ \text{km/sec} \qquad \text{(P-6)}$$

Reference No. 33:

$$p/d = 8.355 \times 10^{-4}\ \rho_p^{2/3}\ \rho_t^{-1/3}\ (V^2/H_t)^{1/3}\ , \qquad V < 9.5\ \text{km/sec} \qquad \text{(P-7)}$$

Reference No. 34:

$$p/d = 2.0\ (\rho_p/\rho_t)^{4.52}\ (V/C)^{1.136}\ , \qquad V < 9\ \text{km/sec} \qquad \text{(P-8)}$$

Reference No. 35:

$$p/d = 0.311\ (\rho_p/\rho_t)^{0.17}\ (\rho_p V^2/S_t)^{0.285} \quad , \qquad V < 7 \text{ km/sec} \qquad \text{(P-9)}$$

Reference No. 36:

$$p/d = 0.36\ (\rho_p/\rho_t)^{2/3}\ (\rho_t V^2/B_t)^{1/3} \quad , \qquad V < 6 \text{ km/sec} \qquad \text{(P-10)}$$

Reference No. 37:

$$p = 2.973 \times 10^{-7}\ d^{1.1}\ H_t^{-0.25} \rho_p^{0.5}\ \rho_t^{-0.167}\ V^{4/3} \quad , \qquad V < \sim 3 \text{ km/sec} \qquad \text{(P-11)}$$

$$p = 1.129 \times 10^{-6}\ d^{1.056}\ H_t^{-0.25}\ \rho_p^{0.5}\ \rho_t^{-0.167}\ E_t^{-0.33}\ V^{4/3} \quad ,$$

$$V < \sim 3 \text{ km/sec} \qquad \text{(P-12)}$$

Crater Diameter Equations

Reference No. 18:

$$\alpha\ d_h^2 p/d^3 = 34\ (\rho_p/\rho_t)^{3/2}\ (V/C)^2 \quad , \qquad V < 4 \text{ km/sec} \qquad \text{(C-1)}$$

Reference No. 35:

$$\alpha\ d_h^2 p/d^3 = 0.120\ (\rho_p/\rho_t)^{0.5}\ (\rho_p V^2/S_t)^{0.845} \quad , \qquad V < 7 \text{ km/sec} \qquad \text{(C-2)}$$

Reference No. 28:

$$\alpha\ d_h^2 p/d^3 = 30.25\ (\rho_p/\rho_t)^{3/2}\ (V/C)^2 \quad , \qquad V < 6 \text{ km/sec} \qquad \text{C-3)}$$

Reference No. 30:

$$\alpha\ d_h^2 p/d^3 = 44.10\ (\rho_p/\rho_t)^{2/3}\ (V/C)^2 \quad , \qquad V < 9 \text{ km/sec} \qquad \text{(C-4)}$$

Reference No. 33:

$$\alpha\ d_h^2 p/d^3 = 2.65 \times 10^{-9}\ \rho_p^{7/6}\ \rho_t^{-1/2}\ V^2/H_t \quad , \qquad V < 9.5 \text{ km/sec} \qquad \text{(C-5)}$$

Reference No. 36:

$$\alpha\, d_h^2 p/d^3 = 0.16\, (\rho_p/\rho_t)^{3/2}\, \rho_p\, V^2/B_t \quad , \qquad V < 6 \text{ km/sec} \qquad \text{(C-6)}$$

Notation

d_h ... crater surface diameter (cm)

d ... projectile diameter (cm)

p ... crater depth (cm)

B_t ... target material Brinell Hardness (dynes/cm^2)

C ... speed of sound in target material (cm/sec)

E_t ... target material elastic modulus (GPa)

H_t ... target material Brinell Hardness Number (kg/mm^2)

S ... target material static shear strength (dynes/cm^2)

S_t ... target material dynamic hardness (dynes/cm^2)

Y_t ... target material dynamic shear strength (dynes/cm^2)

V ... projectile impact velocity

α ... crater shape factor

$\alpha = 0.75$ if $p > d_h/2$

$\alpha = 1.00$ if $p \leq d_h/2$

ρ_p ... projectile material mass density (gm/cm^3)

ρ_t ... target material mass density (gm/cm^3)

σ_{yt} ... target material dynamic yield strength (dynes/cm^2)

Material Properties

$B_t = 1.27 \times 10^{10}$ dynes/cm^2

$C = 5.10 \times 10^5$ cm/sec

$E_t = 7.38 \times 10^{10}$ N/m^2

$S = 2.83 \times 10^9$ dynes/cm^2

$S_t = 6.37 \times 10^{10}$ dynes/cm^2

$Y_t = 2.78 \times 10^9$ dynes/cm^2

$\rho_p = 2.71$ gm/cm^3

$\rho_t = 2.84$ gm/cm^3

$\sigma_{yt} = 1.85 \times 10^{10}$ dynes/cm^2

H_t 130 kg/mm^2

APPROVAL

OBLIQUE HYPERVELOCITY IMPACT RESPONSE OF DUAL-SHEET STRUCTURES

By William P. Schonberg and Roy A. Taylor

The information in this report has been reviewed for technical content. Review of any information concerning Department of Defense or nuclear energy activities or programs has been made by the MSFC Security Classification Officer. This report, in its entirety, has been determined to be unclassified.

RAYMOND L. GAUSE
Chief, Engineering Physics Division

R. J. SCHWINGHAMER for
Director, Materials and Processes Laboratory

☆U.S. GOVERNMENT PRINTING OFFICE: 1969 - 636-085/00052